

Pearl-Vortex Tunneling in Magic-Angle Twisted Graphene

Marta Perego,^{1,*} Peter Koopmann,¹ Clara Galante Agero,¹ Alexandra Mestre Torà,¹ Artem O. Denisov,¹ Takashi Taniguchi,² Kenji Watanabe,³ Vadim Geshkenbein,⁴ Gianni Blatter,^{4,5} Thomas Ihn,^{1,5} and Klaus Ensslin^{1,5}

¹*Laboratory for Solid State Physics, ETH Zurich, CH-8093 Zurich, Switzerland*

²*Research Center for Materials Nanoarchitectonics,*

National Institute for Materials Science, 1-1 Namiki, Tsukuba 305-0044, Japan

³*Research Center for Electronic and Optical Materials,*

National Institute for Materials Science, 1-1 Namiki, Tsukuba 305-0044, Japan

⁴*Institute for Theoretical Physics, ETH Zurich, CH-8093 Zurich, Switzerland*

⁵*Quantum Center, ETH Zurich, CH-8093 Zurich, Switzerland*

(Dated: January 30, 2026)

Twisted graphene provides a tunable platform for studying superconductivity in two dimensions. In the presence of electric currents and magnetic fields, vortices determine the phenomenological properties of the material. Related studies usually address bulk properties averaging over ensembles of vortices. Here, we employ a gate-defined Josephson junction as a single-vortex sensor, enabling direct access to individual vortex dynamical events. Our measurements reveal that, at elevated temperatures ($T > 100$ mK), vortices enter the superconducting leads via classical thermal activation over energy barriers. At lower temperatures ($T < 90$ mK), we observe macroscopic quantum tunneling through these barriers. The data are consistent with a sharp, first-order type quantum-to-classical transition. From our measurements, we extract vortex entry and exit energy barriers on the order of a few Kelvin and estimate the barrier thickness to be approximately 100 nm, corresponding to about one tenth of the device width.

Twisted graphene has recently emerged as a novel superconductor with remarkable tunability: it can be driven into and out of the superconducting state only by changing its carrier density [1–8]. This property enables the realization of superconducting nano-devices within a single material, where adjacent regions can be independently tuned into superconducting, insulating, or metallic phases [9–15]. As a result, twisted graphene provides unprecedented flexibility for device design and in-situ control of electronic phases.

While much of the existing research has focused either on the microscopic origin of superconductivity in twisted graphene [16–20] or on its applications in superconducting electronics [9–15, 21–23], the system also constitutes a powerful new platform to study the phenomenology of superconductivity in two-dimensional (2D) systems. Two-dimensional superconductors exhibit a number of distinctive features, including quasi-long range order [24–27], the Berezinskii-Kosterlitz-Thouless transition [27, 28], and pronounced fluctuation dynamics, here, in the form of topological excitation, i.e., Pearl-vortices [29, 30]. The importance of thermal and quantum fluctuations can be quantified through the superfluid density ρ_s [16, 17] and the sheet resistance R^{\square} . The low carrier density and large effective mass associated with flat electronic bands result in a small ρ_s and a large R^{\square} , which enhance fluctuation effects in both the thermal and quantum regimes. These properties make graphene particularly well suited to study vortex dynamics.

In this work, we focus on dissipative vortex dynamics at low temperatures, where macroscopic quantum fluc-

tuations can directly affect the performance of superconducting devices, including the persistence of currents and the coherent operation of superconducting qubits. Previous studies of macroscopic quantum effects in superconducting junctions have addressed the phase dynamics intrinsic to the Josephson junction itself [31]. Here, by contrast, we study the macroscopic quantum dynamics of individual Pearl-vortices [30] entering or exiting the superconducting leads. In our setup, the (gate-defined) Josephson junction then acts as a single-vortex sensor enabling the detection of the dynamics of individual Pearl-vortices.

As summarized in Fig. 1, we measure the temperature dependence of the vortex entry and exit rates $\Gamma(T)$, see Fig. 1(a), which are governed by Bean-Livingston edge barriers at the film boundaries [32] (Fig. 1(b)). At elevated temperatures ($T > 100$ mK), the rates increase sharply and are well described by classical thermal activation over an energy barrier U , with $\Gamma = \nu_0 \exp(-U/k_B T)$. From this analysis, we extract typical barrier heights $U/k_B \approx 2.6$ K and an attempt frequency $\nu_0 \approx 2.0 \times 10^{11}$ Hz, see the fit in Fig. 1(c). Upon lowering the temperature, the rates saturate at a finite value, with $\ln(\nu_0/\Gamma) \approx 27$, deviating substantially from the extrapolated thermal behavior (Fig. 1(d)). We attribute this saturation to the crossover from thermal activation (TA) to macroscopic quantum tunneling (QT) of Pearl-vortices, in which the thermal exponent $U/k_B T$ is replaced by the dimensionless quantum action S/\hbar . This crossover is indicative of a sharp, first-order like quantum-to-classical transition, consistent with theoretical expectations [33, 34]. In the following sections, we show how these results arise from the observation of telegraph-type switching signals produced by individual

* mperego@phys.ethz.ch

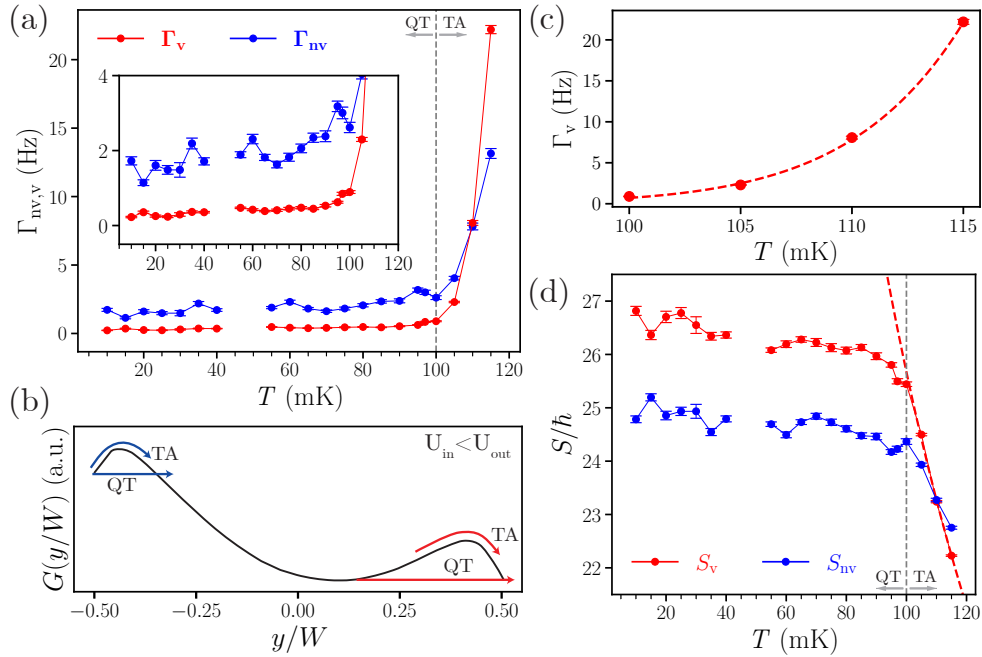


FIG. 1. (a) Temperature evolution of rates $\Gamma(T)$ for vortex-entry into- and vortex-exit out of the superconducting leads. (b) Illustration of the free-energy landscape $G(y/W)$ for vortex motion across the leads. (c) Fitting the sharp rise in $\Gamma(T)$ at $T > 100$ mK with an Arrhenius law, see red dashed line, provides a thermal barrier of height $U/k_B \approx 2.6$ K. (d) The rates saturate at low temperatures to provide a dimensionless action $S/\hbar = \ln(\nu'_0/\Gamma)$ between 24 and 27. The red dashed line extrapolates the thermal activation law $S/\hbar = U/k_B T$.

Pearl-vortices crossing the superconducting leads near the Josephson junction sensor.

Our magic angle twisted four-layer graphene (MAT4G) device, with a twist angle $\theta \approx 1.64^\circ$, consists of an electrostatically defined JJ as studied previously in Ref. 35. A schematic of the device and its characteristic dimensions are presented in Figs. 2, (a) and (b). All measurements are performed with the carrier density and displacement field in the superconducting leads set to $n_l = 4.8 \times 10^{12} \text{ cm}^{-2}$ and $D_l/\epsilon_0 = -0.37 \text{ V/nm}$, respectively, while the junction region is held at $n_j = 6.2 \times 10^{12} \text{ cm}^{-2}$ and $D_j/\epsilon_0 = -0.5 \text{ V/nm}$ (where ϵ_0 denotes the vacuum permittivity). Under these conditions, the leads are tuned to the edge of the superconducting dome, corresponding to the ‘weak-leads’ regime defined in Ref. 35. Owing to the ultra-thin nature of the device, transverse magnetic screening is negligible, and an applied magnetic field H penetrates the film nearly uniformly, such that the magnetic induction within the graphene layers satisfies $B \approx \mu_0 H$ (μ_0 is the vacuum permeability).

When subjecting the device to a perpendicular magnetic field, the maximum (critical) supercurrent $I_c(B)$ across the junction exhibits a pronounced field dependence, forming a characteristic Fraunhofer-like interference pattern (FP) [36, 37]. An example of such a pattern is shown in Fig. 2(c), where the color map is derived from the voltage-current (V - I) characteristics of the junction. Dark and light blue regions correspond to low- and high-differential resistance $R = dV/dI$, respectively, distin-

guishing superconducting ($R = 0$) from flux-flow or normal ($R > 0$) regimes.

In our previous study [35], we observed sharp discontinuities in the Fraunhofer pattern, which we attributed to the entry or exit of individual vortices in the superconducting leads, as indicated by the red arrow in Fig. 2(c). When a vortex enters a lead at $B > 0$, it partially compensates the effect of the applied magnetic field in the vicinity of the junction, thereby reducing its contribution to the Josephson phase. As a result, the Fraunhofer pattern shifts toward higher magnetic fields [38–40], as schematically illustrated in Fig. 2(d); vortex exit produces the opposite shift. These shifts in magnetic field correspond to changes in flux of order of one superconducting flux quantum $\Phi_0 = h/2e = 2.0710^{-15} \text{ Wb}$ over an area of order W^2 . They occur when the vortex manifests sufficiently close to the junction [39]. In measurements performed with the leads tuned to the center of the superconducting dome (the ‘strong-leads’ regime defined in Ref. 35), the energy barriers for vortex motion are large. This results in well-resolved, individually observable jumps in the interference pattern and a slow dynamics due to the formation of metastable states with long lifetimes.

When tuning the device to the ‘weak-leads’ regime, we observe, in addition to quasi-stationary shifts due to long-lived trapped vortex states, a distinct noisy feature in the Fraunhofer interference pattern (see Fig. 4(a) of Ref. [35]). We have attributed this noise to vortices re-

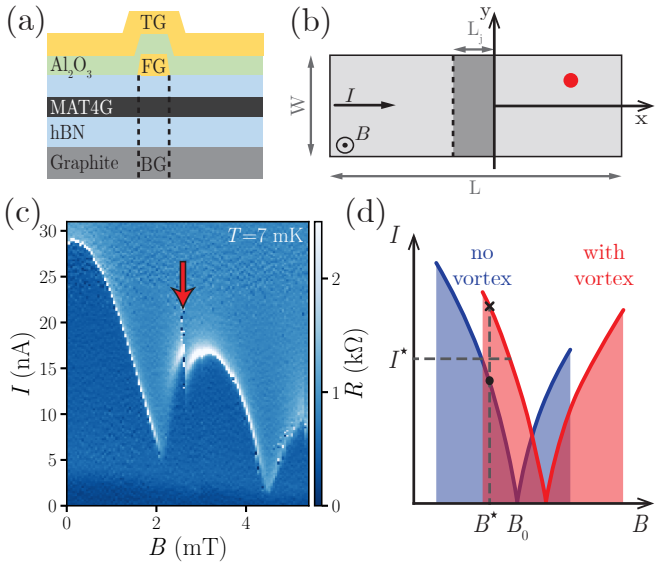


FIG. 2. (a) Layer structure with gates for device tuning, including a graphite bottom gate (BG), a gold top gate (TG), and a gold finger gate (FG) defining the JJ. (b) Device geometry with thickness $d = 1$ nm, width $W = 1.1$ μm along the y -direction, and length $L = 6W$ along x ; the junction width is $L_j = 150$ nm. Vortices penetrate the leads (red dot) and are detected as jumps in the Fraunhofer pattern, see red arrow. (c) The field dependence of the critical current $I_c(B)$ measured at $T = 7$ mK in a film with ‘strong-leads’ tuning assumes the form of a Fraunhofer-like interference pattern (FP), see Ref. 35. A vortex entering a lead produces a sudden rightward shift in the Fraunhofer pattern, see red arrow. (d) Schematic illustrating the change in the dissipation upon vortex entry into a lead: Measuring the voltage V across the junction at fixed current I^* and field $B^* < B_0$, with B_0 the zero of the FP, the response is dissipative when no vortex is present in the lead ($I_c < I^*$), while the junction is superconducting in the presence of a vortex ($I_c > I^*$). The response is reversed when $B^* > B_0$.

peatedly crossing the superconducting leads in the junction vicinity, which causes jumps in the Fraunhofer pattern. This interpretation is supported by measurements of the voltage-current (V - I) characteristics at a fixed magnetic field $B^* = 2$ mT where we observe stochastic switching between two dissipative states, as shown by the red and blue traces in Fig. 3(a). At these elevated temperatures ($T = 100$ mK), the superconducting transition is rounded and no sharp critical current can be identified. Upon cooling to $T = 7$ mK while maintaining $B^* = 2$ mT, a well-defined critical current I_c emerges and the switching occurs between superconducting (red) and dissipative (blue) states, as shown in Fig. 3(b).

We interpret these jumps between distinct V - I traces as arising from the entry and exit of individual Pearl-vortices in the superconducting leads. At high temperatures, the applied field B^* lies to the right of the zero of the Fraunhofer pattern located at B_0 ($B^* > B_0$), such that vortex entry enhances dissipation. At low tempera-

tures, B^* falls below B_0 ($B^* < B_0$, see Fig. 2(d)) and the entry of a vortex shifts the junction into the superconducting state producing a downward jump in V - I . This is followed by an upward jump upon vortex exit with the junction going back to the original state.

By measuring the time-dependent voltage $V(t)$ across the junction at fixed field $B^* \approx 2$ mT and current $I^* \approx 4$ nA, we observe consecutive voltage jumps consistent with the behavior described above. At elevated temperatures $T = 100$ mK, see Fig. 3(c), we observe segments exhibiting a telegraph-type switching between high- (red) and low-dissipative (blue) levels. These ‘switching segments’, typically lasting on the order of ~ 100 s, are interspersed with longer ‘silent segments’ (cyan) of duration ~ 1000 s. We interpret this superstructure in $V(t)$ as arising from an additional quasi-stationary vortex that enters or exits the superconducting leads on a longer time scale. A detailed discussion of this behavior will be presented in a forthcoming publication [41].

At low temperatures, the red-blue segments in the voltage trace $V(t)$ are interrupted by cyan segments that now exhibit telegraph-type switching as well, visible as orange spikes in Fig. 3(d), which shows a representative section of $V(t)$ measured at $T = 7$ mK. In this regime, the zero of the Fraunhofer pattern has shifted to the right of the measurement field ($B_0 > B^*$), and we therefore associate the superconducting states (orange and red) with a vortex traversing the lead, while the dissipative states (cyan and blue) correspond either to vortex-free conditions or to the presence of a quasi-stationary vortex.

The interchange of low- and high-dissipation states associated with the presence or absence of a vortex appears around a temperature $T \approx 45$ mK where B_0 matches the measurement field B^* , $B_0 \approx B^*$. The disappearance of the orange spikes in the cyan-orange segments with increasing temperature is explained by a decreasing vortex passage time τ_v . Once τ_v drops below the resolution limit of the detector (with bandwidth $f_{\text{BW}} \approx 1.1$ kHz), the fast dynamics can no longer be resolved, and the cyan segment appears ‘silent’.

In the statistical analysis of voltage traces with a total duration of 4 hours, we extract the waiting times for vortex entry, τ_{nv} , and exit, τ_v . Specifically, we define τ_{nv} as the time interval without a vortex in the lead and τ_v as the time during which a vortex is present. The digitized time traces are analyzed using a dedicated algorithm [42], from which the two-state waiting times are identified and extracted. These waiting times are subsequently binned into histograms using the Freedman-Diaconis rule [43]. The vortex entry and exit rates, Γ_{nv} and Γ_v , are obtained by fitting exponential distributions. Depending on the type of segment, red-blue or orange-cyan, the pairs of waiting times $[\tau_{\text{nv}}^i, \tau_v^i]$ associated with the passage of the i -th vortex typically differ by about one order of magnitude. As a result, the data are best described by a bi-exponential model, with all rates corrected for the finite detector bandwidth [44]. In the following, we focus on the red-blue segments.

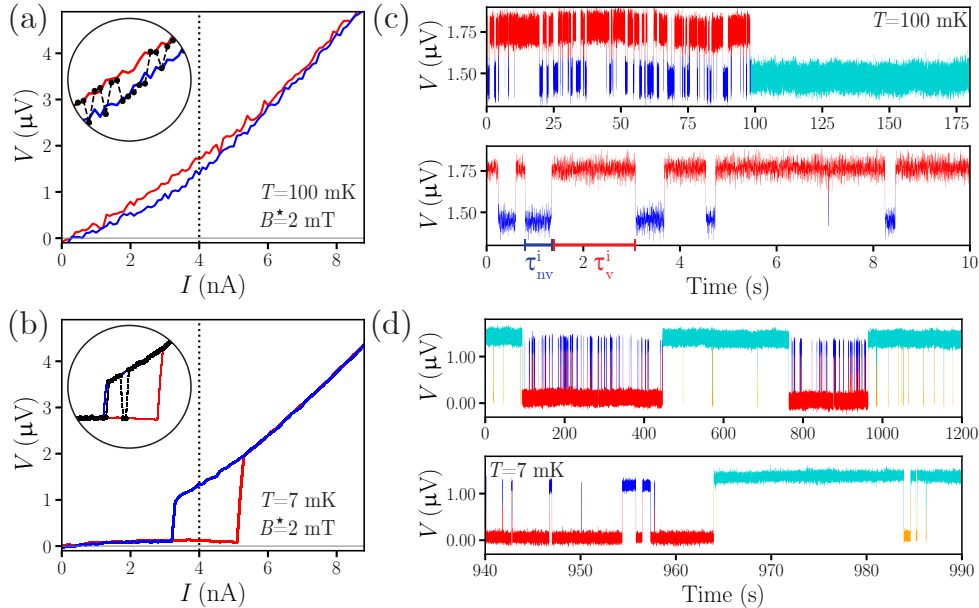


FIG. 3. (a) V - I voltage-current characteristic at $B^* = 2$ mT and high temperature $T = 100$ mK with low- (blue) and high-dissipative (red) traces. Vortices traversing the leads produce switching between the two states, see blowup. (b) The same at $T = 7$ mK where the V - I characteristic exhibits a sharp critical current I_c . (c) Time trace $V(t)$ of the voltage across the junction taken at $B^* = 2$ mT and $I^* = 4$ nA, see dotted line in (a). The trace $V(t)$ exhibits segments with switching events (red–blue) due to the passage of vortices across one of the leads; these ‘switching segments’ are interrupted by ‘silent’ ones (cyan). (d) The same at $T = 7$ mK with the previously ‘silent segments’ (cyan in (c)) now exhibiting jumps to the superconducting state (orange).

The temperature dependence of the extracted vortex entry and exit rates Γ_{nv} and Γ_v is shown in Fig. 1(a). Overall, both rates, Γ_{nv} and Γ_v , decrease steeply with decreasing temperature and saturate at a constant value below $T \approx 100$ mK. At high temperatures ($T > 120$ mK), the detector performance is limited by thermal noise, while the absence of data points near $T \approx 45$ mK, where $B^* \approx B_0$, is due to a loss of resolution.

We interpret our experimental results within a theoretical framework based on the free-energy landscape $G(y; H, I)$ [45] that vortices experience as they are driven across the leads by the applied current I , as illustrated in Fig. 1(b). Vortex penetration into the leads is hindered by an edge barrier, that is progressively lowered by the applied magnetic field H , while the transport current I introduces a tilt to the free-energy landscape. For a homogeneous thin film in the weak screening limit, where the magnetic induction satisfies $B \approx \mu_0 H$, the free energy takes the form [46]

$$G(y; H, I) = \varepsilon_0 d \left[\ln \left(\frac{2W}{\pi \xi} \cos \left(\frac{\pi y}{W} \right) \right) + 0.38 \right] - \varepsilon_0 d \frac{\pi}{2} \frac{\mu_0 H W^2}{\Phi_0} \left(1 - \frac{4y^2}{W^2} \right) - I \frac{\Phi_0 y}{W}, \quad (1)$$

as depicted schematically in Fig. 1(b). Here, $\varepsilon_0 = (4\pi/\mu_0)(\Phi_0/4\pi\lambda_L)^2$ is the vortex line energy, λ_L and ξ are the London penetration- and coherence lengths. In our device, the potential landscape depends on the 2D

position $\mathbf{R} = (x, y)$ within the film due to finite sample size (along x) and inhomogeneities, e.g., the superstructure due to the layer twist or defects and impurities.

At high temperatures, vortices attempting to penetrate (leave) the superconducting leads need to overcome the edge energy barrier U_{nv} (U_v). Assuming that *thermal activation* drives the vortices over the barriers, we relate the measured rates $\Gamma_{\text{nv},v}$ to the microscopic parameters $U_{\text{nv},v}$,

$$\Gamma_{\text{nv},v}(T) = \nu_0 \exp(-U_{\text{nv},v}/k_B T), \quad (2)$$

with ν_0 the attempt frequency. Making use of the rates $\Gamma_{\text{nv},v}(T)$ at high temperatures, we find barriers for vortex entry and exit in the Kelvin range. For example, analyzing the temperature dependence of the rate $\Gamma_v(T)$ shown in Fig. 1(a) in the range 100 mK $< T < 120$ mK, we extract $U_v/k_B \approx 2.6$ K and $\nu_0 \approx 2 \times 10^{11}$ Hz, with the latter value in agreement with previous estimates [47, 48].

The rates $\Gamma_{\text{nv},v}$ saturate to constant values upon decreasing the temperature below $T \approx 100$ mK as seen in Fig. 1(a). This phenomenon is naturally explained in terms of *macroscopic quantum tunneling* [49–51]. In this regime, the thermal exponential $U/k_B T$ in Eq. (2) has to be replaced by the dimensionless quantum action S/\hbar , such that the rates become

$$\Gamma_{\text{nv},v} = \nu'_0 \exp(-S_{\text{nv},v}/\hbar), \quad (3)$$

with $S_{\text{nv},v}$ denoting the Euclidean action for vortex entry and exit. Replotting the data for the rates $\Gamma_{\text{nv},v}$ in

terms of the dimensionless action $S_{\text{nv},n}/\hbar = \ln(\nu'_0/\Gamma_{\text{nv},n})$ as shown in Fig. 1(d), we find nearly constant values between 24 – 27 at low temperatures $T < 100$ mK (we assume an attempt rate $\nu'_0 = \nu_0 \sim 2.0 \times 10^{11}$ Hz). The values decrease with increasing T as thermal fluctuations assist the tunneling dynamics [33, 50] at higher temperatures.

The barrier height U for the thermal activation of vortices over the edge barrier is $U \approx \alpha_U \varepsilon_0 d$, with α_U of order unity as follows from Eq. (1) and Ref. [35]. The vortex dynamics in a superconductor are dominated by the friction coefficient $\eta_l = \Phi_0^2/2\pi\xi^2\rho_n$, where ρ_n is the normal-state resistivity [52]. The vortex tunneling action then is given by [50]

$$S = \alpha_s \eta_l d q_b^2 = \frac{\alpha_s}{4} \hbar \left(\frac{q_b}{\xi} \right)^2 \frac{R_K}{R^\square} \quad (4)$$

and depends on the barrier width $\sim q_b$ rather than its height U . Here, $R_K = h/e^2 \approx 25.8$ k Ω is the von-Klitzing constant and $R^\square = \rho_n/d$ denotes the film resistance. For a metastable potential in the form of a cubic parabola,

$$V(q) = 3U \left[\left(\frac{q}{q_b} \right)^2 - \frac{2}{3} \left(\frac{q}{q_b} \right)^3 \right] \quad (5)$$

the numerical prefactor is $\alpha_s = \pi/2$ [50]. Using these expressions for the barrier height and tunneling action, we extract relevant phenomenological parameters of the superconductor. With the experimentally determined value $U/k_B \approx 2.6$ K, we infer a London penetration depth of order $\lambda_L \approx 2.7$ μ m. The sheet resistance of the film is $R^\square \approx 2$ k Ω , and the coherence length is $\xi \approx 40$ nm [35]. Combining these values with the expression for S , we obtain a tunneling distance $(3/2)q_b \approx W/8 \approx 3.5\xi$, in good agreement with the typical barrier thickness extracted from the free-energy landscape in Eq. (1).

Figure 1(d) shows the full temperature dependence of the dimensionless action $S(T)/\hbar$. For the metastable cubic parabola, this dependence has been calculated previously [50] and is given by

$$\frac{S(T)}{\hbar} = \frac{S_0}{\hbar} \left[1 - \frac{2}{3} \left(\frac{T}{T_0} \right)^2 \right], \quad (6)$$

quadratically decreasing with temperature T to a value $(2/3)S_0/\hbar = U/k_B T_0$ at the crossover temperature T_0 . For temperatures above T_0 , the action crosses over to the purely thermal form $S(T \geq T_0)/\hbar = U/k_B T$. Our experimental results in Fig. 1(d) deviate from this prediction in two respects. First, the measured action remains approximately constant, $S(T) \approx S_0$ rather than decreasing by $S_0/3$ as expected upon approaching $T_0 \approx 100$ mK. Second, for a metastable cubic parabola the dissipative decay is predicted to exhibit a smooth, second-order type transition at T_0 [33, 50]. Instead, in our data, the transition appears markedly sharper.

These features of $S(T)$ are not universal, but depend strongly on both the particle dynamics—whether massive

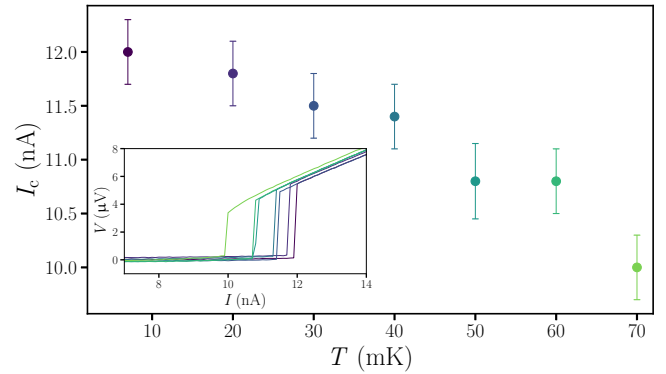


FIG. 4. Critical current I_c at $B = 0$ mT as a function of temperature T obtained from the sharp V – I characteristics shown in the inset; the characteristics becomes rounded at higher temperatures $T > 70$ mK.

or dissipative—and on the shape $V(q)$ of the metastable potential. For example, for a massive particle in a cubic metastable potential, the action $S(T)$ decreases by only a small fraction, $1 - 10\pi/36 \approx 0.13$, up to the (smooth) crossover at T_0 [53]. Regarding the potential's shape, the curvature of $V(q)$ at the minimum governs the initial decrease of $S(T)$ with increasing temperature T , whereas the curvature at the barrier top determines the crossover temperature T_0 . Moreover, modifications in the overall shape of $V(q)$ can change the order of the transition, as discussed for the massive case in Ref. [34].

The free energy landscape $G(y)$ of a Pearl-vortex in a thin film differs qualitatively from the shape of a cubic parabola. It rises steeply near the edges due to vortex–anti-vortex separation arising from image effects and exhibits a relatively flat maximum, in contrast to the cubic parabola which has equal curvatures in the minimum and at the barrier maximum. These differences lead us to expect a reduced temperature dependence of $S(T)$ and open the possibility of a first-order like transition. While quantitative results are available for massive particle dynamics [34], a corresponding analysis for the dissipative case remains to be done. Addressing this problem, together with a more accurate calculation of the free energy landscape $G(y)$ for vortex entry and exit beyond the London approximation, constitute interesting problems for future work.

In conclusion, we have studied vortex dynamics in magic-angle twisted graphene using a gate-defined Josephson junction as a single-vortex sensor. This transport-based method enables the detection of individual vortices and their real-time dynamics. We attribute the observed telegraph-type switching to vortices traversing the superconducting leads, with thermal activation over edge barriers giving way to macroscopic quantum tunneling as switching rates saturate upon decreasing temperature. While such saturation to macroscopic quantum tunneling is often subject to skepticism—for example, due to potential failures in temperature equilibra-

tion at low temperatures—the persistence of a clear temperature dependence in the junction critical current $I_c(T)$ down to our lowest measurement temperature (Fig. 4) confirms that the device is well equilibrated. Our results provide guidance for the design and operation of sensitive superconducting devices, such as qubits and quantum sensors, where vortex fluctuations have a detrimental impact.

DATA AVAILABILITY

The data supporting the findings of this study, together with the code for plotting the figures, is available online through the ETH Research Collection at <https://doi.org/10.3929/ethz-c-000794076>.

ACKNOWLEDGMENTS

We thank Peter Märki and the staff of the ETH cleanroom facility FIRST for technical support. We acknowledge fruitful discussions with Vladimir Kogan. Financial support was provided by the European Graphene Flagship Core3 Project, H2020 European Research Council (ERC) Synergy Grant under Grant Agreement 951541, the European Union’s Horizon 2020 research and innovation program under grant agreement number 862660/QUANTUM E LEAPS, the European Innovation Council under grant agreement number 101046231/FantastiCOF, the EU Cost Action CA21144 (SUPERQUMAP), and NCCR QSIT (Swiss National Science Foundation, grant number 51NF40-185902). K.W. and T.T. acknowledge support from the JSPS KAKENHI (Grant Numbers 21H05233 and 23H02052) and the World Premier International Research Center Initiative (WPI), MEXT, Japan. C.G.A. acknowledges support from the Heidi Ras foundation via

an ETH Quantum Center fellowship.

Author contributions

M.P. fabricated the device. T.T. and K.W. supplied the hBN crystals. M.P., P.K. and C.G.A. performed the measurements. M.P. and P.K. analysed the data. V.G. and G.B. developed the theoretical model. M.P. and G.B. wrote the manuscript, and all authors were involved in the reviewing process. M.P., P.K., C.G.A. and A.M.T. discussed the data. M.P., V.G., G.B., K.E. and T.I. conceived and designed the experiment. T.I. and K.E. supervised the work.

Appendix A: Fabrication details

We fabricated a MAT4G stack using the dry pick-up method [54]. All the details for the fabrication and tuning of this sample can be found in [35].

Appendix B: Measurement setup

All measurements were carried out in a dilution refrigerator with a base temperature of 7 mK. Our measurements are current biased, i.e., we apply a current and measure the voltage drop in a two-terminal configuration (we correct for contact resistances). To generate the bias current, we use a home-built d.c. source in series with a 10 M Ω or 100 M Ω resistor. The measured voltage is amplified using a home-built low-noise d.c. amplifier (see [55]) and its output is measured with a Hewlett Packard 3441A digital multimeter. The bottom, top, and finger gates are connected to home-built low-noise d.c. voltage sources. For the statistical analysis of vortex fluctuations, the output voltage is further amplified (gain x30k), low-pass filtered at 1.1 kHz and recorded in time using a National Instruments BNC-2110 data acquisition card (DAQ) with a sampling frequency of 20 kHz.

[1] Y. Cao, V. Fatemi, A. Demir, S. Fang, S. L. Tomarken, J. Y. Luo, J. D. Sanchez-Yamagishi, K. Watanabe, T. Taniguchi, E. Kaxiras, *et al.*, Correlated insulator behaviour at half-filling in magic-angle graphene superlattices, *Nature* **556**, 80 (2018).

[2] X. Lu, P. Stepanov, W. Yang, M. Xie, M. A. Aamir, I. Das, C. Urgell, K. Watanabe, T. Taniguchi, G. Zhang, *et al.*, Superconductors, orbital magnets and correlated states in magic-angle bilayer graphene, *Nature* **574**, 653 (2019).

[3] Y. Cao, V. Fatemi, S. Fang, K. Watanabe, T. Taniguchi, E. Kaxiras, and P. Jarillo-Herrero, Unconventional superconductivity in magic-angle graphene superlattices, *Nature* **556**, 43 (2018).

[4] J. M. Park *et al.*, Tunable strongly coupled superconductivity in magic-angle twisted trilayer graphene, *Nature* **590**, 249 (2021).

[5] Z. Hao, A. Zimmerman, P. Ledwith, E. Khalaf, D. H. Najafabadi, K. Watanabe, T. Taniguchi, A. Vishwanath, and P. Kim, Electric field-tunable superconductivity in alternating-twist magic-angle trilayer graphene, *Science* **371**, 1133 (2021).

[6] J. M. Park *et al.*, Robust superconductivity in magic-angle multilayer graphene family, *Nature Materials* **21**, 877 (2022).

[7] Y. Zhang, R. Polski, C. Lewandowski, A. Thomson, Y. Peng, Y. Choi, H. Kim, K. Watanabe, T. Taniguchi, J. Alicea, *et al.*, Promotion of superconductivity in

magic-angle graphene multilayers, *Science* **377**, 1538 (2022).

[8] G. W. Burg, E. Khalaf, Y. Wang, K. Watanabe, T. Taniguchi, and E. Tutuc, Emergence of correlations in alternating twist quadrilayer graphene, *Nature Materials* **21**, 884 (2022).

[9] D. Rodan-Legrain, Y. Cao, J. M. Park, S. C. de la Barrera, M. T. Randeria, K. Watanabe, T. Taniguchi, and P. Jarillo-Herrero, Highly tunable junctions and non-local Josephson effect in magic-angle graphene tunnelling devices, *Nature Nanotechnology* **16**, 769 (2021).

[10] F. K. de Vries, E. Portolés, G. Zheng, T. Taniguchi, K. Watanabe, T. Ihn, K. Ensslin, and P. Rickhaus, Gate-defined Josephson junctions in magic-angle twisted bilayer graphene, *Nature Nanotechnology* **16**, 760 (2021).

[11] J. Díez-Mérida, A. Díez-Carlón, S. Yang, Y.-M. Xie, X.-J. Gao, J. Senior, K. Watanabe, T. Taniguchi, X. Lu, A. P. Higginbotham, *et al.*, Symmetry-broken Josephson junctions and superconducting diodes in magic-angle twisted bilayer graphene, *Nature Communications* **14**, 2396 (2023).

[12] E. Portolés, S. Iwakiri, G. Zheng, P. Rickhaus, T. Taniguchi, K. Watanabe, T. Ihn, K. Ensslin, and F. K. de Vries, A tunable monolithic SQUID in twisted bilayer graphene, *Nature Nanotechnology* **17**, 1159 (2022).

[13] Y. Ronen, V. Bhardwaj, L. Rajagopal, L. Arici, M. Bocarsly, A. Ilin, G. Shavit, K. Watanabe, T. Taniguchi, Y. Oreg, and T. Holder, Competing Orbital Magnetism and Superconductivity in electrostatically defined Josephson Junctions of Alternating Twisted Trilayer Graphene, unpublished (2025).

[14] S. Iwakiri, A. Mestre-Torà, E. Portolés, M. Visscher, M. Perego, G. Zheng, T. Taniguchi, K. Watanabe, M. Sigrist, T. Ihn, *et al.*, Tunable quantum interferometer for correlated moiré electrons, *Nature Communications* **15**, 390 (2024).

[15] G. Zheng, E. Portolés, A. Mestre-Torà, M. Perego, T. Taniguchi, K. Watanabe, P. Rickhaus, F. K. de Vries, T. Ihn, K. Ensslin, *et al.*, Gate-defined superconducting channel in magic-angle twisted bilayer graphene, *Physical Review Research* **6**, L012051 (2024).

[16] A. Banerjee, Z. Hao, M. Kreidel, P. Ledwith, I. Phinney, J. M. Park, A. Zimmerman, M. E. Wesson, K. Watanabe, T. Taniguchi, *et al.*, Superfluid stiffness of twisted trilayer graphene superconductors, *Nature* **638**, 93 (2025).

[17] M. Tanaka, J. Î.-j. Wang, T. H. Dinh, D. Rodan-Legrain, S. Zaman, M. Hays, A. Almanaky, B. Kannan, D. K. Kim, B. M. Niedzielski, *et al.*, Superfluid stiffness of magic-angle twisted bilayer graphene, *Nature* **638**, 99 (2025).

[18] E. Portolés, M. Perego, P. A. Volkov, M. Toschini, Y. Kemna, A. Mestre-Torà, G. Zheng, A. O. Denisov, F. K. d. Vries, P. Rickhaus, *et al.*, Quasiparticle and superfluid dynamics in Magic-Angle Graphene, *Nature Communications* **16**, 1 (2025).

[19] F. Wu, E. Hwang, and S. Das Sarma, Phonon-induced giant linear-in-T resistivity in magic angle twisted bilayer graphene: Ordinary strangeness and exotic superconductivity, *Physical Review B* **99**, 165112 (2019).

[20] M. Oh, K. P. Nuckolls, D. Wong, R. L. Lee, X. Liu, K. Watanabe, T. Taniguchi, and A. Yazdani, Evidence for unconventional superconductivity in twisted bilayer graphene, *Nature* **600**, 240 (2021).

[21] A. Rothstein, A. Fischer, A. Achtermann, E. Icking, K. Hecker, L. Banszerus, M. Otto, S. Trelenkamp, F. Lentz, K. Watanabe, *et al.*, Gate-Defined Single-Electron Transistors in Twisted Bilayer Graphene, *Nano Letters* **25**, 6429 (2025).

[22] R. Jha, M. Endres, K. Watanabe, T. Taniguchi, M. Banerjee, C. Schönenberger, and P. Karnatak, Large tunable kinetic inductance in a twisted graphene superconductor, *Physical Review Letters* **134**, 216001 (2025).

[23] A. Díez-Carlón, J. Díez-Mérida, P. Rout, D. Sedov, P. Virtanen, S. Banerjee, R. P. S. Penttilä, P. Altpeter, K. Watanabe, T. Taniguchi, S.-Y. Yang, K. T. Law, T. T. Heikkilä, P. Törmä, M. S. Scheurer, and D. K. Efetov, Probing the Flat-Band Limit of the Superconducting Proximity Effect in Twisted Bilayer Graphene Josephson Junctions, *Phys. Rev. X* **15**, 041033 (2025).

[24] T. M. Rice, Superconductivity in One and Two Dimensions, *Phys. Rev.* **140**, A1889 (1965).

[25] N. D. Mermin and H. Wagner, Absence of Ferromagnetism or Antiferromagnetism in One- or Two-Dimensional Isotropic Heisenberg Models, *Phys. Rev. Lett.* **17**, 1133 (1966).

[26] P. C. Hohenberg, Existence of Long-Range Order in One and Two Dimensions, *Phys. Rev.* **158**, 383 (1967).

[27] V. L. Berezinskii, Destruction of Long-range Order in One-dimensional and Two-dimensional Systems having a Continuous Symmetry Group I. Classical Systems, *Soviet Journal of Experimental and Theoretical Physics* **32**, 493 (1971).

[28] J. M. Kosterlitz and D. J. Thouless, Ordering, metastability and phase transitions in two-dimensional systems, *Journal of Physics C: Solid State Physics* **6**, 1181 (1973).

[29] A. A. Abrikosov, On the magnetic properties of superconductors of the second group, [Zh. Eksp. Teor. Fiz. **32**, 1442 (1957)] *JETP* **5**, 1174 (1957).

[30] J. Pearl, Current distribution in superconducting films carrying quantized fluxoids, *Applied Physics Letters* **5**, 65 (1964).

[31] M. H. Devoret, J. M. Martinis, and J. Clarke, Measurements of Macroscopic Quantum Tunneling out of the Zero-Voltage State of a Current-Biased Josephson Junction, *Phys. Rev. Lett.* **55**, 1908 (1985).

[32] C. P. Bean and J. D. Livingston, Surface Barrier in Type-II Superconductors, *Physical Review Letters* **12**, 14 (1964).

[33] I. Affleck, Quantum-Statistical Metastability, *Phys. Rev. Lett.* **46**, 388 (1981).

[34] E. M. Chudnovsky, Phase transitions in the problem of the decay of a metastable state, *Physical Review A* **46**, 8011 (1992).

[35] M. Perego, C. Galante Agero, A. Mestre Torá, E. Portolés, A. O. Denisov, T. Taniguchi, K. Watanabe, F. Gagiolli, V. Geshkenbein, G. Blatter, T. Ihn, and K. Ensslin, Experimental detection of vortices in magic-angle graphene, *Nature Communications* **16**, 10259 (2025).

[36] M. Tinkham, *Introduction to Superconductivity* (Dover Publications, Mineola, NY, 2004).

[37] J. R. Clem, Josephson junctions in thin and narrow rectangular superconducting strips, *Physical Review B* **81**, 144515 (2010).

[38] J. R. Clem, Effect of nearby Pearl vortices upon the I_c versus B characteristics of planar Josephson junctions in thin and narrow superconducting strips, *Phys. Rev. B* **84**, 134502 (2011).

[39] V. Kogan and R. Mints, Interaction of Josephson junction and distant vortex in narrow thin-film superconducting strips, *Physical Review B* **89**, 014516 (2014).

[40] V. Kogan and R. Mints, Manipulating Josephson junctions in thin-films by nearby vortices, *Physica C* **502**, 58 (2014).

[41] M. Perego *et al.*, Vortex Dynamics in Magic-Angle Twisted Graphene, in preparation (2026).

[42] Y. Yuzhelevski, M. Yuzhelevski, and G. Jung, Random telegraph noise analysis in time domain, *Review of Scientific Instruments* **71**, 1681 (2000).

[43] D. Freedman and P. Diaconis, On the histogram as a density estimator : L_2 theory, *Zeitschrift für Wahrscheinlichkeitstheorie und Verwandte Gebiete* **57**, 453 (1981).

[44] O. Naaman and J. Aumentado, Poisson Transition Rates from Time-Domain Measurements with a Finite Bandwidth, *Phys. Rev. Lett.* **96**, 10.1103/PhysRevLett.96.100201 (2006).

[45] G. Stejic, A. Gurevich, E. Kadyrov, D. Christen, R. Joynt, and D. C. Larbalestier, Effect of geometry on the critical currents of thin films, *Phys. Rev. B* **49**, 1274 (1994).

[46] The derivation of Eq. (1) considers the situation in a parallel field, that can be adopted to the present situation by the appropriate replacing of the thickness d with the width W .

[47] A. P. Malozemoff and M. P. A. Fisher, Universality in the current decay and flux creep of Y-Ba-Cu-O high-temperature superconductors, *Phys. Rev. B* **42**, 6784 (1990).

[48] V. Kopylov *et al.*, The role of surface effects in magnetization of high-Tc superconductors, *Physica C* **170**, 291 (1990).

[49] A. O. Caldeira and A. J. Leggett, Quantum tunnelling in a dissipative system, *Annals of physics* **149**, 374 (1983).

[50] A. Larkin and Y. N. Ovchinnikov, Quantum-mechanical tunneling with dissipation. the pre-exponential factor, *Zh. Eksp. Teor. Fiz.* **86**, 726 (1984).

[51] L. Glazman and N. Y. Fogel', Possibility of quantum tunneling of vortices in thin superconducting films, *Soviet Journal of Low Temperature Physics* **10**, 51 (1984).

[52] J. Bardeen and M. Stephen, Theory of the motion of vortices in superconductors, *Physical Review* **140**, A1197 (1965).

[53] U. Weiss, *Quantum Dissipative Systems (2nd edition)* (World Scientific Publishing, Singapore, 1999).

[54] K. Kim, M. Yankowitz, B. Fallahazad, S. Kang, H. C. P. Movva, S. Huang, S. Larentis, C. M. Corbet, T. Taniguchi, K. Watanabe, S. K. Banerjee, B. J. LeRoy, and E. Tutuc, van der Waals Heterostructures with High Accuracy Rotational Alignment, *Nano Letters* **16**, 1989 (2016).

[55] P. Märki, B. A. Braem, and T. Ihn, Temperature-stabilized differential amplifier for low-noise DC measurements, *Review of Scientific Instruments* **88**, 10.1063/1.4997963 (2017).